Structural, vibrational and photoluminescence properties of Sr(1-x)PbxMoO4 solid solution synthesized by solid state reaction

Abdelali Hallaoui, A. Taoufyq, Madjid Arab, Bahcine Bakiz, Abdeljalil Benlhachemi, Lahcen Bazzi, Jean-Christophe Valmalette, Sylvie Villain, Frédéric Guinneton, Jean-Raymond Gavarri

Structural, vibrational and photoluminescence properties of $Sr_{(1-x)}Pb_xMoO_4$ solid solution synthesized by solid state reaction

A. Hallaoui[a,b], A. Taoufyq[a,b], M. Arab[a], B. Bakiz[b], A. Benlhachemi[b], L. Bazzi[b], J-C. Valmalette[a], S. Villain[a], F. Guinneton[a], J-R. Gavarri[a,*]

[a] *IM2NP, UMR CNRS 7334, University of Toulon, BP20132, 83957 La Garde, France*
[b] *LME, Faculty of Sciences, University Ibn Zohr, 80000 Agadir, Morocco*

In this paper, strontium lead molybdate $Sr_{1-x}Pb_xMoO_4$ polycrystalline samples with $0 \leq x \leq 1$ were prepared by solid state preparation method at 1000 °C. These materials were characterized by X-ray diffraction (XRD), scanning electron microscopy (SEM), and micro-Raman spectroscopy. Their photoluminescence responses were analyzed under X-ray excitation. Rietveld refinements indicate that all the materials present a scheelite-type tetragonal structure. Micro-Raman spectra confirmed the formation of the solid solution with a specific effect due to Sr-O-Mo and Pb-O-Mo links in the scheelite structure. SEM images showed modifications in the shapes and grain sizes as x increased. Broad photoluminescent emission bands were observed in the energy range 2.1–2.9 eV. The emission bands were decomposed into four gaussian components. The intensities of all components presented a strong maximum in the composition range $0.1 < x < 0.4$.

1. Introduction

In recent years, tungstates and molybdates have attracted a great deal of interests due to their broad potential to industrial application, including optic fiber, humidity sensor, catalysts, scintillation detector, solid-state lasers, photoluminescent devices and microwave applications [1–26]. Molybdates are significant luminescent materials with scheelite-type tetragonal structure, $I4_1/a$ space group, with two formula units per primitive cell. The scheelite structures $MMoO_4$ are characterized by a juxtaposition of $[MoO_4]$ tetrahedra and $[MO_8]$ hexahedra [27–31], with chemical links M-O-Mo. The pure molybdate phases $MMoO_4$ were synthesized from various methods: flux method [32], Czochralski technique [33,34], floating zone-like technique [35], co-precipitation process [36–40], sonochemical [41,42], citrate complex method [43,44], hydrothermal technique [45–50], solvothermal routines [51–57], microemulsion method [58], microwave-assisted synthesis method [59,60] and solid state reaction [61]. The two pure strontium and lead molybdate phases were previously synthesized by solid state reaction [62], flux [63], Czochralski [64], co-precipitation [65], hydrothermal [66] and pulsed laser ablation method [67].

Presently, we deal with the modifications of properties of solid solutions $A_{1-x}B_x(Mo, W)O_4$: in these materials, the atoms A and B (or Mo and W) can be distributed on the same crystallographic site, in ordered or disordered way. A high crystallization level of each compound can be reached (regular lattice) after specific synthesis method, despite the existence of a full disorder of atoms on their sites. In the case of luminescence properties of solid solutions, this disorder can play a prominent role in emission intensities.

Recently, photoluminescence properties in solid solutions $Sr_{1-x}Pb_xWO_4$, $Ca_{1-x}Cd_xWO_4$ and $Ba_{1-x}Sr_xMoO_4$ ceramics were analyzed as a function of the composition x [1–3,68]. The general aim was to better understand the role of substitution in the photoluminescence of tungstates and molybdates. The phase diagram of the $SrMoO_4$-$PbMoO_4$ system was partly determined by Zhuravlev et al. [69]. In our previous work on this system under X-ray excitation, we observed a significant increase of emission intensities in the range x = 0.2 to 0.4. Therefore in this paper, a new study of this molybdate based solid solution, we try to better understand the role of substitution on photoluminescence in molybdate materials. A series $Sr_{1-x}Pb_xMoO_4$ has been synthesized and characterized using X-ray diffraction (XRD), Raman spectroscopy (RS), and scanning electron microscopy (SEM). Finally, the photoluminescence properties (PL) have been analyzed under X-ray excitation.

* Corresponding author.
E-mail address: gavarri.jr@univ-tln.fr (J.-R. Gavarri).

2. Experimental details

2.1. Synthesis by solid state method

Several series of eleven samples $Sr_{(1-x)}Pb_xMoO_4$ with $0 \leq x \leq 1$, were prepared by conventional solid state chemical reaction using polycrystalline precursors MoO_3 [Sigma-Aldrich N° 1313-27-5, >99.5%], $SrCO_3$ [Sigma-Aldrich No. 1633-05-2, >99.0%] and PbO [Sigma-Aldrich No. 1317-36-8, >99.0%]. The elaboration conditions (grinding process, temperature and time of thermal treatment) were optimized to reach a high crystallization level. The final process was as follows: the reagents in stoichiometric proportions were thoroughly mixed and ground in an agate mortar for 15 min, then thermally treated at 600 °C for 3 h, in pure alumina crucible under air. The samples were ground again, thoroughly for 2 h, and then retreated at 1000 °C for 6 h, under air. The main difficulty in this synthesis is the high volatility of PbO and MoO_3. A 1.5 wt% and 2 wt% excess amounts of MoO_3 and PbO respectively were added to the mixture to compensate for the volatilization of MoO_3 and PbO during synthesis of the polycrystalline powders.

2.2. X-ray diffraction analyses

Each sample was analyzed by X-ray diffraction using an Empyrean Panalytical diffractometer, equipped with a copper X-ray source (wavelength $\lambda = 1.54.10^{-10}$ m, tension V = 45 kV, intensity I = 35 mA), and with a Ni filter eliminating the Kβ radiation. The diffractometer was equipped with a Pixcel-1D-Detector. The XRD analysis was carried out using the classical θ–2θ configuration, in continuous mode, with a step size of 0.00164, a scan speed of 0.002/s. All polycrystalline samples were compacted in a specific sample holder.

The structural parameters of the samples were refined using the Fullprof software [70] based on Rietveld procedure. The experimental profiles were fitted with the most suitable pseudo-Voigt analytical function. For both $K\alpha_1$ and $K\alpha_2$ profiles, the line broadening function and the symmetric part of instrumental function may be represented by the pseudo-Voigt (pV) function:

$$pV(x) = \sum I_{nt}[\eta L(x) + (1-\eta)G(x)] \quad (1)$$

In this expression, $L(x) = (1+x^2)^{-1}$ is the Lorentzian component, and $G(x) = \exp[(\ln 2)\, x^2]$ is the Gaussian component, $x = (2\theta - 2\theta_0)/FWHM$ (FWHM = Full Width at Half Maximum of the Bragg peaks), η is the gaussian character of X-ray profiles, θ_0 the Bragg angle of $K\alpha_1$ peak and I_{nt} is the scale factor. Considering the integrated intensity of the peaks as a function of structural parameters only, the Marquardt least-squares procedures were used to minimize the difference between the observed and simulated powder diffraction patterns. The minimization was carried out using the reliability index parameters such as Bragg factors (R_{Bragg}) comparing the calculated and observed intensities ($I_{i_{cal}}$ and $I_{i_{obs}}$), R_F factors comparing the calculated and observed structure factors ($F_{i_{obs}}$ and $F_{i_{cal}}$), and expected factors R_{exp}. All these parameters were used to characterize the quality of the fit between calculated and experimental diffraction profiles. The main reliability factors are defined as follows:

$$R_{Bragg_{(\%)}} = 100_{(\%)} \cdot \frac{\sum_i |I_{i_{obs}} - I_{i_{cal}}|}{\sum_i I_{i_{obs}}} \quad (2)$$

$$R_{F_{(\%)}} = 100_{(\%)} \cdot \left\{ \frac{\sum_i |I_{i_{obs}} - I_{i_{cal}}|}{\sum_i \sqrt{I_{i_{obs}}}} \right\} \quad (3)$$

$$R_{exp_{(\%)}} = 100_{(\%)} \cdot \left[\frac{n-p}{\sum_i w_i \left(y_{i_{obs}}\right)^2} \right]^{1/2} \quad (4)$$

In these expressions, $y_{i(obs)}$ is the intensity of experimental profile for a given 2θ angle, $w_i = (1/y_{i_{obs}})$ is the weight of profile determination, n is the number of experimental observations and p is the number of fitting parameters. A detailed description of the mathematical procedures implemented in the Rietveld analysis has been earlier reported by Rietveld and Pradhan et al. [71–75].

We used the atom coordinates obtained by Nogueira et al. on $SrMoO_4$ [76] and by authors Gurmen et al. on $PbMoO_4$ [77], to initiate the refinements of the various structures. The coordinates of oxygen atoms of intermediate compounds ($0 < x < 1$) were determined by interpolation, using the oxygen coordinates of $SrMoO_4$ and $PbMoO_4$; then these coordinates were fixed during the refinement procedure (see section results 2.2, below). These coordinates cannot be refined because of the high difference of scattering factors of oxygen and heavy atoms (Sr, Pb, Mo). The coordinates of W and average M (Sr, Pb) atoms were fixed because they occupy particular Wyckoff positions in the space group of scheelite structures. The average atoms M were considered as a mix of the Sr and Pb atoms with occupancy factors fixed by composition x. Cell parameters and Debye-Waller (DW) factors of heavy atoms were refined.

2.3. Scanning electron microscopy analysis

A systematic analysis of grain sizes and morphologies was performed using a Supra 40 Vp Colonne Gemini Zeiss scanning electron microscope (SEM), with a maximum voltage of 20 kV. Local chemical analysis using an Oxford EDS X-Max system, with a spatial resolution of 0.1 μm was carried out to control the homogeneity of powders.

2.4. Micro-Raman spectroscopy analysis

Raman spectroscopy was used to analyze the effect of substitution on vibration modes, and to correlate these vibration modes with the structural evolutions. The equipment used to record the various vibration spectra was a spectrometer Horiba Jobin-Yvon HR800 LabRam, spatially resolved to 0.5 μm, by means of an optical microscope with a 100X objective. The latter has a dual function: it allows firstly focusing the laser beam on a small area, and, secondly, visualizing the area of the sample. The 514.5 nm line of an Ar-ion laser was used as the excitation source; the photonic power applied to the samples was limited to 5 μW with an acquisition time of 30 s. Each Raman emission band was characterized by its wavenumber (in cm^{-1}).

2.5. Luminescence experiments analysis

The copper X-ray source of the diffractometer Empyrean (Panalytical) was used to irradiate the samples and perform luminescence experiments. The nominal emission conditions (voltage V_{RX}/current I_{RX}) were 45 kV/35 mA. The resulting excitation energies ranged between 0 and 45 000 eV, with a maximum located at about 20 000 eV. It should be noted that the X-ray source also delivered the classical transition energies of copper source. All samples were in form of 2 mm thick cylindrical pellets, compacted under a pressure of 5 kbars, placed at a constant distance of the X-ray source, set with a fixed distance to the incident X-ray beam of about 10 cm. The luminescence emissions of samples were recorded using a UV – visible spectrophotometer MicroHR (Jobin

Yvon) equipped with an optical fiber of 400 μm in diameter. The fiber was set at a fixed distance of the sample surfaces (1 mm), with a fixed inclination of 55° with respect to the sample surface. The constant dimensions of the rectangular surfaces of irradiated grains were of about 2 mm/20 mm. Experiments with voltages V_{RX} varying from 10 to 45 kV and filament current I_{RX} varying between 10–35 mA, were also performed.

3. Results and discussion

3.1. X-ray diffraction analyses

The XRD patterns of Fig. 1 indicate that the $Sr_{1-x}Pb_xMoO_4$ solid solution was formed after annealing at 1000 °C. As composition x increases, the positions of the Bragg peaks shift slightly to smaller 2θ angles. All Bragg peaks were indexed in the scheelite tetragonal structure with space group $I4_1/a$. No other phase was observed in the diffraction patterns.

The refinement procedure was as follows:

- The M (Sr,Pb) and Mo positions were fixed as a result of space group;
- The individual Debye Waller (DW) factors of heavy atoms were refined;
- The DW factors of oxygen were fixed;
- The oxygen positions were calculated as a function of composition x considering that they can be interpolated using the positions of authors Gurmen et al. and Nogueira et al.: each oxygen coordinate was calculated by linear interpolation:

$$O(x) = (1-x)\cdot O_{SrMoO4} + xO_{PbMoO4}x \quad (1)$$

where O_{SrMoO4} and O_{PbMoO4} represent the oxygen positions (x_{Ox}, y_{Ox}, z_{Ox}) in the two limit structures of $SrMoO_4$ and $PbMoO_4$. Such approximation is justified by the linear variations of cell parameters, suggesting ideal nature of solid solution.

Table 1 reports the refined structural parameters. The results reported in Table 1 are in agreement with the ones found in the literature for pure molybdates $SrMoO_4$ [76] and $PbMoO_4$ [78]. Fig. 2 shows a selected result (x = 0.5) comparing calculated diffraction profiles to experimental data.

The main results of these refinements reside in the quasi-linear increase of cell parameters and volume as x increases: the solid solution behaves as an ideal one. The high crystallization level is validated by the FWHM's of all Bragg peaks, as a function of x.

The a and c parameters, the cell volume V, vary with x in agreement with Vegard law (Fig. 3a and b):

$$a(x) = b(x) = 5.397 + 0.040.x\ (\pm 0.001)\ \text{in Å} \quad (2a)$$

$$c(x) = 12.029 + 0.080.x\ (\pm 0.001)\ \text{in Å} \quad (2b)$$

$$V(x) = 350.34 + 7.60.x\ (\pm 0.05)\ \text{in (Å)}^3 \quad (2c)$$

Having regard to large standard deviations (due to experiment and Rietveld procedure), the Debye Waller (DW) factor B(x) associated with the average site M (Sr, Pb) follows a linear evolution:

$$B(x) = 0.12 + 0.23.x\ (\pm 0.05)\ \text{in (Å)}^2. \quad (3)$$

The B(x) values represent the static displacements of M (Sr, Pb) atom positions as Pb substitutes for Sr. These static displacements can play also the role of a correcting factor compensating incorrect oxygen positions. The invariance of the DW factor of Mo (B = 0.5 $Å^2$) atoms (Fig. 4) argues in favor of fixed position of this atom in this structure. Finally, the disorder could be described in terms of rotations of tetrahedra MoO_4 (the Mo positions being fixed) and disordered displacements of M atoms due to juxtaposed links Sr-O-Mo and Pb-O-Mo.

From these Rietveld analyses, it was possible to extract the main bond lengths and bond angles. We report the significant characteristics in Table 2 (limited to x = 0, 0.5 and 1). It should be noted that the Mo-O distances in MoO_4 tetrahedra slowly vary from 1.73 Å for $SrMoO_4$ to 1.77 Å for $PbMoO_4$, while the M-O distances in MO_8 groups are quasi constant as a function of x. Small variations in angles are observed. In MoO_4 tetrahedra and MO_8 groups, several angles slowly vary as a function of x. The angles M-O-Mo characterizing the links between M cations and centers of tetrahedra.

3.2. Micro-Raman spectra

Micro-Raman spectra were described using the classical attributions of vibration modes of scheelite structures [79–81]. In scheelite structures, the Raman bands can be divided into two groups, constituted of internal and external vibration modes. The internal vibration modes correspond to the vibrations within the $[MoO_4]^{2-}$ anions. The external modes are associated to the motion of the Pb^{2+} or Sr^{2+} cations and the rigid molecular unit. The

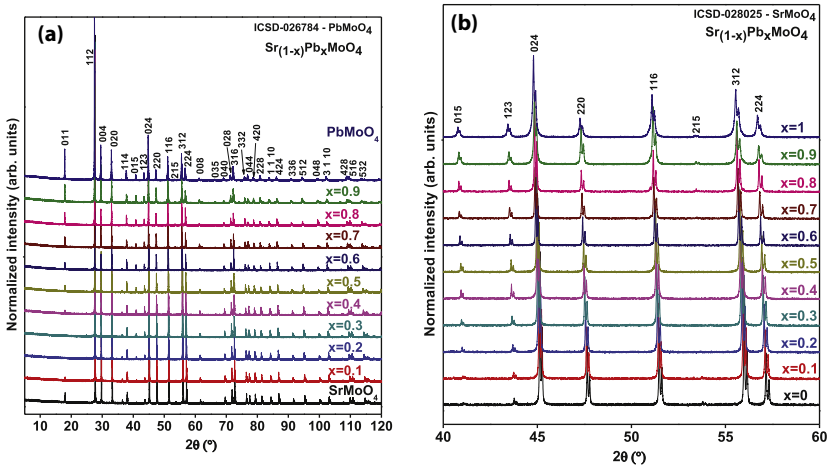

Fig. 1. (a) XRD patterns of the tetragonal $Sr_{1-x}Pb_xMoO_4$ powders, $0 \le x \le 1$.; (b) Zoom in the 2θ angle range 40–60.

Table 1
Structural parameters for solid solution $Sr_{1-x}Pb_xMoO_4$ $0 \leq x \leq 1$.

x	0	0.1	0.2	0.3	0.4	0.5
a (10^{-10} m)	5.39685(2)	5.40064 (2)	5.40465 (1)	5.40889 (2)	5.41285 (2)	5.41776 (2)
b (10^{-10} m)	5.39685(2)	5.40064 (2)	5.40465 (1)	5.40889 (2)	5.41285 (2)	5.41776 (2)
c (10^{-10} m)	12.02906(7)	12.03645 (5)	12.04424 (5)	12.05297 (5)	12.05967 (5)	12.06961 (5)
Volume Cell (10^{-30} m^3): V	350.359 (3)	351.066 (2)	351.815 (2)	352.622 (2)	353.336 (2)	354.268 (2)
B (M) = ($8\pi^2/3$). $<\Delta r^2>$ (Å^2)	0.26 (6)	0.10 (5)	0.19 (4)	0.18 (5)	0.17 (6)	0.20 (6)
B (W) (Å^2)	0.44 (5)	0.47 (6)	0.54 (5)	0.51 (5)	0.57 (6)	0.54 (3)
O (x.y.z)	x: 0.23180	x: 0.23214	x: 0.23248	x: 0.23282	x: 0.23316	x: 0.23350
	y: 0.11359	y: 0.11357	y: 0.11355	y: 0.11353	y: 0.11351	y: 0.11349
	z: 0.04630	z: 0.04607	z: 0.04584	z: 0.04561	z: 0.04538	z: 0.04515
W (x.y.z)	Fixed values: x = 0.00000; y = 0.25000; z = 0.12500 (**)					
M (x.y.z)	Fixed values: x = 0.00000; y = 0.25000; z = 0.62500 (**)					
Reliability factors (*)						
R_B %	3.88	4.23	5.56	4.50	8.20	8.72
R_F (%)	6.12	5.86	6.00	5.43	7.21	8.44
R_{exp} (%)	4.89	6.04	6.35	6.58	6.79	7.16

x	0.6	0.7	0.8	0.9	1.0
a (10^{-10} m)	5.42119 (2)	5.42515 (2)	5.42903 (2)	5.43288 (3)	5.43664 (3)
b = a (10^{-10} m)	5.42119 (2)	5.42515 (2)	5.42903 (2)	5.43288 (3)	5.43664 (3)
c (10^{-10} m)	12.07675 (5)	12.08454 (5)	12.09248 (5)	12.09919 (7)	12.10911 (10)
Volume Cell (10^{-30} m^3): V	354.928 (2)	355.676 (2)	356.418 (2)	357.122 (4)	357.909 (4)
B (M) = ($8\pi^2/3$). $<\Delta r^2>$ (Å^2)	0.19 (6)	0.21 (7)	0.36 (5)	0.32 (6)	0.44 (6)
B (W) (Å^2)	0.49 (7)	0.43 (6)	0.46 (6)	0.53 (7)	0.51 (4)
O (x.y.z)	x: 0.23384	x: 0.23418	x: 0.23452	x: 0.23486	x: 0.23520
	y: 0.11348	y: 0.11346	y: 0.11344	y: 0.11342	y: 0.11340
	z: 0.04492	z: 0.04469	z: 0.04446	z: 0.04423	z: 0.04400
W (x.y.z)	Fixed values: x = 0.00000; y = 0.25000; z = 0.12500 (**)				
M (x.y.z)	Fixed values: x = 0.00000; y = 0.25000; z = 0.62500 (**)				
Reliability	6.85	8.26	9.43	8.10	9.12
factors (*)	7.43	7.80	6.89	6.47	6.87
R_B %	7.38	7.58	7.23	7.49	7.74
R_F (%)					
R_{exp} (%)					

Notes: (*)$R_B = 100.\{\sum|I_k^{obs} - I_{ki}^{calc}|\sum|I_k^{obs}|\}$; $R_F = 100.\{\sum w_i|(I_{iobs})^{1/2}\text{-}(I_{ical})^{1/2}|/\sum(I_{iobs})^{1/2}|\}$; $R_{exp} = 100.\{[(N-P)/\sum w_i|y_i^{obs}|^2]^{1/2}\}$ where N, P are the number of observations and parameters respectively. (**) Sr, Pb. Mo and O coordinates from author [76,77] have been fixed. Oxygen coordinates for substituted samples were interpolated.

$[MoO_4]^{2-}$ tetrahedra, with T_d symmetry in the free space, can be divided into four internal modes denoted by $\boldsymbol{\nu}_1$(A1), $\boldsymbol{\nu}_2$(E), $\boldsymbol{\nu}_3$(F2) and $\boldsymbol{\nu}_4$(F2), one free rotation mode (F_1) and one translation mode (F_2). Based on the character of the point-group symmetry, optically active modes in Raman (R) and infrared (IR) spectra are represented in Eq. (4):

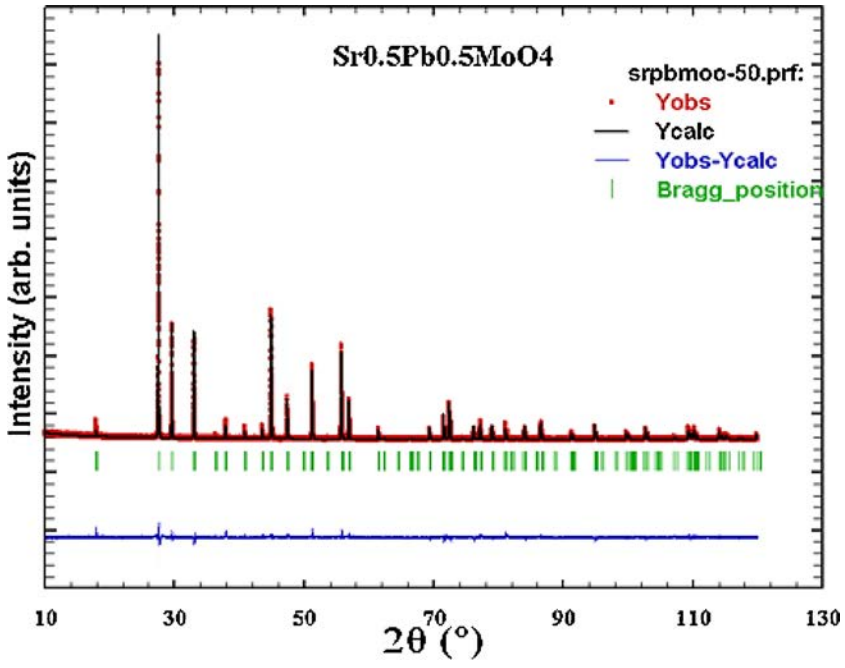

Fig. 2. Calculated and observed diffraction profiles from Rietveld analyses for the $Sr_{0.5}Pb_{0.5}MoO_4$ phase. Y_{calc}: calculated profile and Y_{obs}: observed profile.

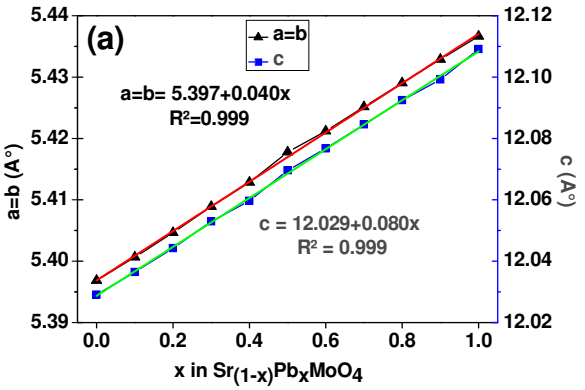

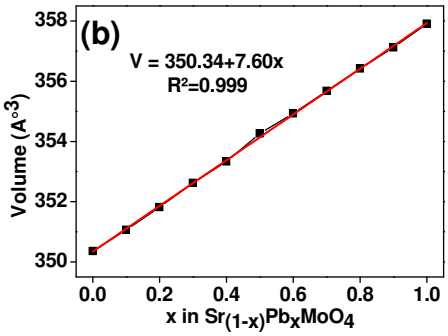

Figure 3b:

Fig. 3. a Variations of cell parameters a and c (Å). b Variation of cell volume.

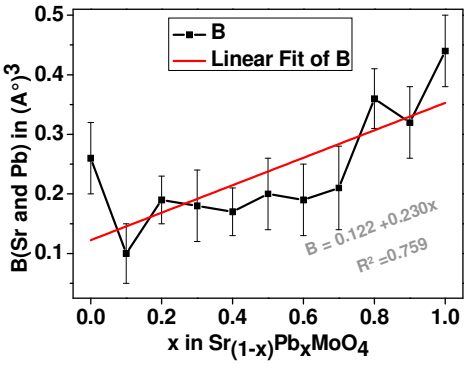

Fig. 4. Variation of the Debye–Waller factor B of M ($Sr_{(1-x)}Pb_x$) vs composition x in $Sr_{(1-x)}Pb_xMoO_4$.

$$\Gamma = 3A_g + 5A_u + 5B_g + 3B_u + 5E_g + 5E_u \quad (4)$$

The even vibrations (A_g, B_g and E_g) are Raman active while the odd modes ($4A_u$ and $4E_u$) are IR active. The three B_u vibrations are silent modes; one A_u and one E_u are acoustic vibrations [76,82]. Among the 13 Raman active vibration modes, seven are internal modes of the $[MoO_4]^{2-}$ tetrahedra, and the remaining six are external modes: two rotations with A_g symmetry and four translations with $2B_g$ and $2E_g$ symmetries. The internal vibrations of the $[MoO_4]^{2-}$ are generally expected to have higher wavenumbers than the ones of the translational vibrations of Sr/Pb and $[MoO_4]^{2-}$.

However, in this study, we observed only 10 Raman-active modes. Fig. 5 reports the various Micro-Raman spectra corresponding to 2 A_g, 5 B_g and 3 E_g vibrational modes. Three other Raman peaks (1 A_g, 2 E_g) which are not observed can overlap with other peaks.

In Table 3 we have reported the various vibration modes observed as x increases.

The Raman wavenumbers decrease linearly with composition x. This is mainly due to a mass effect (Pb mass > Sr mass) associated with a decrease of the force constants of Mo-O bonds probably related to the small increase of bond lengths with composition x (see Table 2). The wavenumber of the A_g mode linked to symmetric vibrations of tetrahedra varies as follows: $\nu(A_g) = 887 - 18.x$ (± 0.19) in cm^{-1}. The variations of the A_g, E_g and B_g vibration modes are shown on Fig. 6.

The profiles of all Raman bands are systematically broadened for substituted samples. This is clearly illustrated by the evolution with x of the FWHM of the A_g mode (887 cm^{-1}), on Fig. 7. This can be ascribed to a disorder increasing with x, resulting from the juxtaposition of Sr-O and Pb-O bonds and more precisely from strong local distortions due this juxtaposition. The FWHM's are small for $SrMoO_4$ and large for $PbMoO_4$. In this last sample, the strong intensities are characteristic of increasing covalence due to Pb-O bonds. This covalence could be associated with the increasing bond lengths Mo-O in the tetrahedra.

A specific analysis of two characteristic E_g and B_g modes delivered additional informations on the disorder in this solid solution. These vibration modes are characterized by wavenumbers of 794 (E_g) and 845 (B_g) cm^{-1} for x = 0, and by wavenumbers of 743 (E_g) and 767 (B_g) cm^{-1} for x = 1. For intermediate compositions, we clearly observe a shift of both E_g and B_g wavenumbers to weaker values, associated with a modification of profiles and intensities of each band. For substituted compounds, the vibrational component E_g splits into a doublet, with variable intensities of the doublet as a function of x. This evolution is characteristic of a strong disorder in the structures of substituted phases: this can be described through the juxtaposition of the two types of links Sr-O-Mo and Pb-O-Mo involving two types of orientations of tetrahedra MoO_4 in the lattice. As Pb composition increases, the mass effect and the difference in force constants are at the origin of the wavenumber shift, while the difference in angles "Sr-O-Mo" and "Pb-O-Mo" should be at the origin of the splitting of E_g mode.

3.3. Scanning electron microscopy

The SEM analyses reported on Fig. 8a–k showed that the as-prepared powders generally consisted of a complex distribution of different grain sizes. A progressive evolution of morphologies and grains sizes is observed as x increases. In Fig. 8a–e, we have inserted magnified images, to better illustrate the morphologies. In the range $0 < x < 1$ the morphologies and sizes can be described as follows:

- In the composition range $0.1 < x < 0.4$, a majority of large and regular crystallites presenting well-defined edges is observed: these crystallites present grain boundaries with smooth morphologies.
- For x = 0.4 and x = 0.5, the grains exhibit a complex size distribution and diversified morphologies.
- For compositions x = 0.6 and x = 0.7 a majority of the grains having edges and facets contains holes.
- For compositions x > 0.8, a mix system of crystallites with large and small grains with large crystallites covered by smaller grains, is observed.

Table 4 reports the chemical analysis of grains and the determination of grain sizes as a function of composition x. We observe a regular increase of grain sizes as x increases.

Table 2
Bond angles and Bond distances (in Å) extracted from Rietveld Analysis.

	$SrMoO_4$	$Sr_{0.5}Pb_{0.5}MoO_4$	$PbMoO_4$
Distances Mo-O (Å) in MoO_4	1.733	1.754	1.774
Angles in MoO_4 (°)	107.4	107.6	107.8
	113.8	113.3	112.9
Distances M-O (Å)	2.616	2.617	2.610
Groups MO_8 M = Sr/Pb	2.624	2.625	2.634
Angles in MO_8 groups in (°)	67.7	67.7	67.7
O-M-O	73.4	73.7	73.9
	76.5	76.6	76.7
	78.8	78.6	78.2
	79.1	79.0	79.1
	93.5	93.6	93.7
	97.5	97.7	98.0
	105.4	105.2	105.1
	111.9	111.9	111.9
	125.5	125.7	125.8
	128.1	128.0	127.9
	137.6	136.9	136.3
	148.6	149.0	149.4
Angles M-O-Mo	121.36	120.75	120.13
	135.08	135.23	135.38
O—O	2.79	2.83	2.86
	3.90	3.95	3.97

3.4. Luminescence

The luminescence spectra obtained under X-ray excitation are presented in Fig. 9a–k. Commonly, the luminescence of the molybdates excited with photons with energies exceeding the band gap value consists of a broad peak with the maximum at 490–550 nm [83]. The band gap values of $SrMoO_4$ and $PbMoO_4$ are well known to be close to $E_{gap}(Sr) = 3.98$ eV and $E_{gap}(Pb) = 3.3$ eV, respectively [31,80]. As our structural and vibrational analyses have clearly shown that the compounds of the series $Sr_{1-x}Pb_xMoO_4$ present the character of a disordered solid solution, we can expect that the corresponding band gaps E(x) will have intermediate values $E_{gap}(Pb) < E(x) < E_{gap}(Sr)$. It is generally admitted that the emission spectrum of the metal molybdates is mainly due to the charge transfers within the $[MoO_4]^{2-}$ complexes [84,85]. According to Bi et al. the conduction bands of $SrMoO_4$ and $PbMoO_4$ are dominated by Mo 4d states and some contributions of Pb (or Sr) and O atoms are also observed. However, it is worthwhile to note that the components of the top of valence band are different. For $SrMoO_4$, like many metal oxides, the top of the valence band is mainly derived from O 2p states. However, the top of the valence band of $PbMoO_4$ consists of not only O 2p but also Pb 6s states, indicating the obvious covalent interactions between Pb and O atoms [86]. In the case of $PbMoO_4$, several authors assume that the lead electronic states 6s-6p could participate to the observed electronic transitions, given the fact that the Pb6s orbital is located just below the valence band [47,82,87].

Our PL spectra of Fig. 9a–k have been decomposed into four Gaussian components (G_1, G_2, G_3 and G_4) to achieve a good agreement with the experimental data. Each component was characterized by its intensity (surface of gaussian curve) and the energy of the centroid of the gaussian. Similar decompositions were proposed for the solid solutions of tungstates $Ca_{1-x}Cd_xWO_4$ and $Sr_{1-x}Pb_xWO_4$ [1,2].

The G1 peak is centered in the yellow wavelength region (2.1 eV), the G2 gaussian is positioned in the green region (2.4 eV), the G3 gaussian is situated in the blue region (2.65 eV) and the G4 occupied the violet-blue region (2.9 eV). Each component represents a different type of electronic transition, which can be linked with the structural arrangement and/or surface defects.

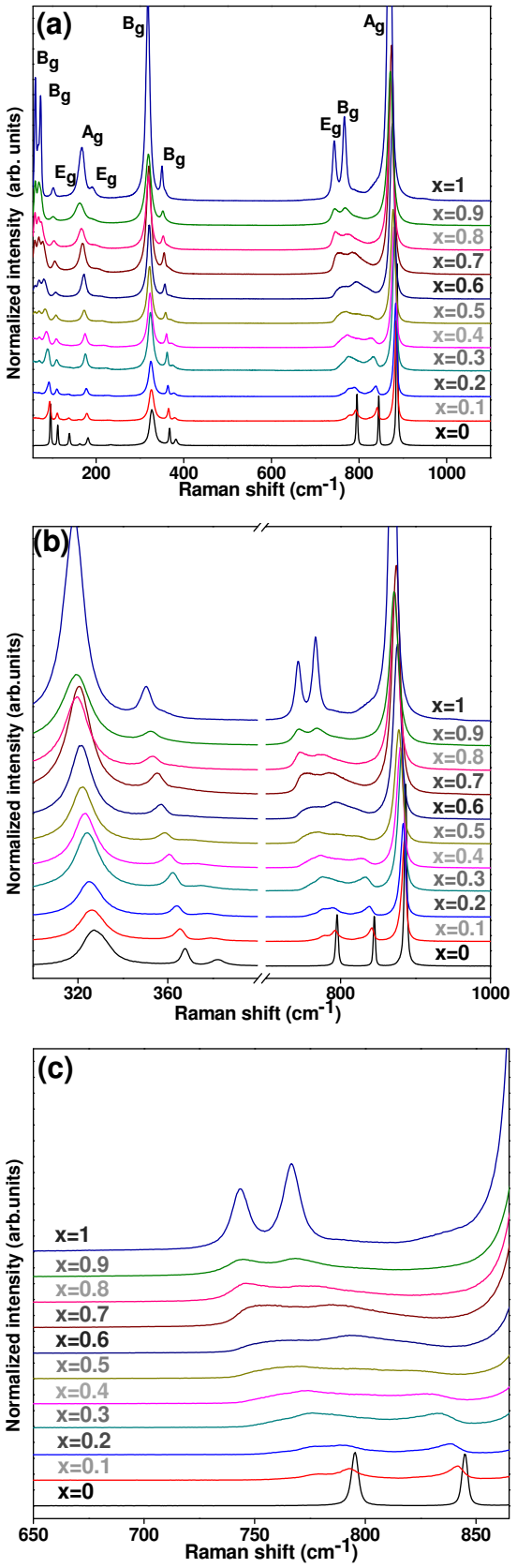

Fig. 5. (a) Room temperature Raman spectra of $Sr_{1-x}Pb_xMoO_4$, for $0 \leq x \leq 1$, (b) Zoom in the number wave domain 325–1000 cm-1(c) Zoom in of the Eg and Bg modes (λ (excit.) = 514.5 nm).

Table 3
Micro-Raman spectroscopy data of $Sr_{1-x}Pb_xMoO_4$ solid solution with $0 \leq x \leq 1$. (fitted with Lorentzian and Gaussian functions).

	Bg	Bg	Eg	Ag	Eg	Bg	Bg	Eg	Bg		Ag
x = 0	(*)	96.18	112.49	181.43	234.06	327.60	367.66	(*)	794.13	844.86	886.76
x = 0.1	69.53	94.22	111.45	178.83	228.49	326.24	365.26	778.03	785.11	840.36	885.08
x = 0.2	69.59	92.17	110.53	177.68	226.47	325.23	363.78	775.00	780.60	837.46	883.54
x = 0.3	69.79	89.13	110.10	175.69	222.64	324.07	362.03	761.77	773.19	832.95	881.47
x = 0.4	70.28	86.66	109.50	174.75	216.80	323.19	360.58	755.87	770.13	826.99	879.84
x = 0.5	70.43	83.76	108.59	172.64	212.75	321.90	358.14	751.41	762.72	814.91	877.73
x = 0.6	69.99	81.22	107.73	172.08	209.84	321.33	356.74	744.08	756.76	795.58	875.82
x = 0.7	68.87	78.61	105.92	169.08	202.75	320.47	354.97	(*)	752.25	786.56	874.21
x = 0.8	68.17	76.36	104.23	168.30	200.31	319.38	353.11	(*)	746.29	777.70	872.19
x = 0.9	68.08	74.10	103.94	167.43	192.91	318.25	351.41	(*)	744.84	768.68	870.27
x = 1	67.92	73.50	102.03	166.24	191.58	317.25	350.28	(*)	743.23	767.23	869.61
$\Delta\nu/\nu$	(*)	0.02	0.28	0.09	0.07	0.19	0.03	(*)	0.07	0.10	0.03

Note: ν = Raman shift in cm^{-1}; $\Delta\nu/\nu = [\nu(x=1) - \nu(x=0)]/\nu(x=1)$.

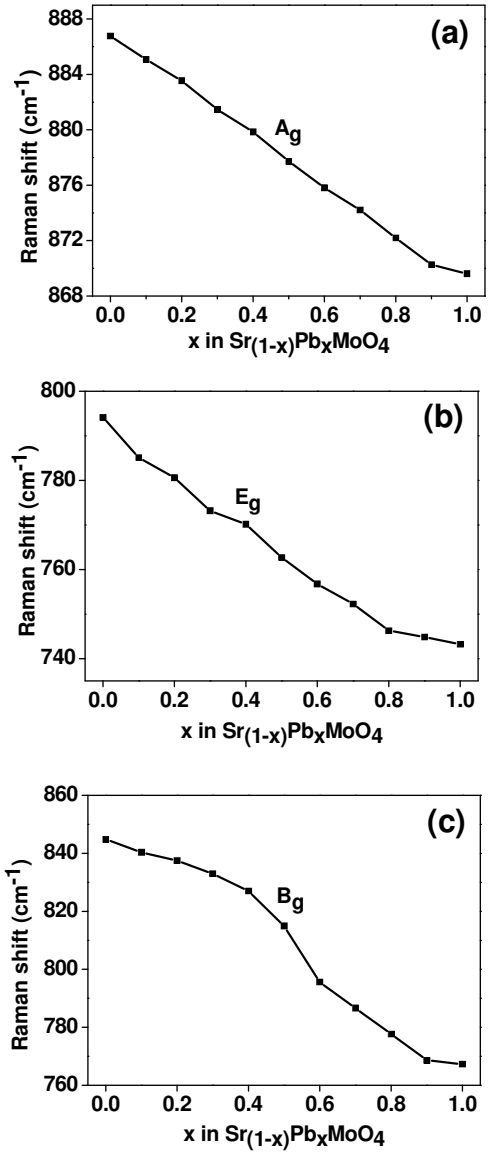

Fig. 6. (a) Variation of wavenumbers with composition x of the symmetric A_g mode; (b) and (c) Variation of wavenumbers with x of the asymmetric Eg and Bg modes.

On Fig. 10(a,a′–e,e′), we have reported the energies and intensities of the G_1 to G_4 components and of the global spectra, as a function of composition x.

The main features can be summarized as follows:

- All components are characterized by a similar strong increase of intensities in the composition range $0.2 < x < 0.5$, with maxima located close to x = 0.3;
- The G1 component (yellow) is characterized by a quasi-constant energy (2.15 eV) with a small decrease for x = 1;
- The G2 component (green) is characterized by a constant energy E = 2.38 eV (±0.1 eV);
- The G3 component (blue) exhibits a decrease in energy from 2.65 to 2.45 eV;
- The G4 component (violet-blue) is characterized by a constant energy close to 2.91 eV (±0.1 eV).

If we refer to the theoretical calculations of *Bacci* et al. [88], these components could be due to the splitting of configuration energies, involved by the distortions of regular tetrahedra. In the present case, such distortions could be justified by the disorder of Sr-O-Mo and Pb-O-Mo links (see the Raman analysis above) involving local rotations and distortions of these tetrahedra. In such conditions the two $^3T_1, ^3T_2 \rightarrow {}^1A_1$ spin forbidden ($\Delta S = 1$) transitions proposed by authors *Groenink and Blasse* [89,90] and *Chen and Gao* [91] should split into 4 transitions.

The origins of these transitions were extensively discussed in the literature. By the past, different authors considered that these emissions were directly associated with MoO_4^{2-} groups (ions). Sczancoski et al. reported that the blue PL emission in $PbMoO_4$ microcrystals, as well as its intensity variations, could be explained by a model based on both distorted [MoO_4] and [PbO_8] clusters in

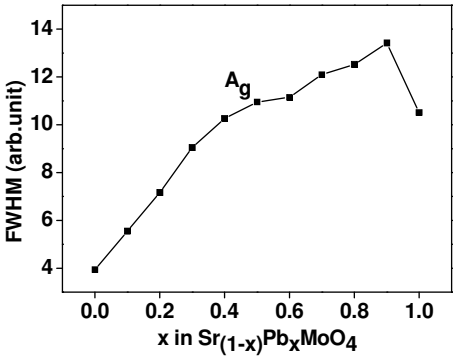

Fig. 7. Variation with x of the FWHM of A_g mode.

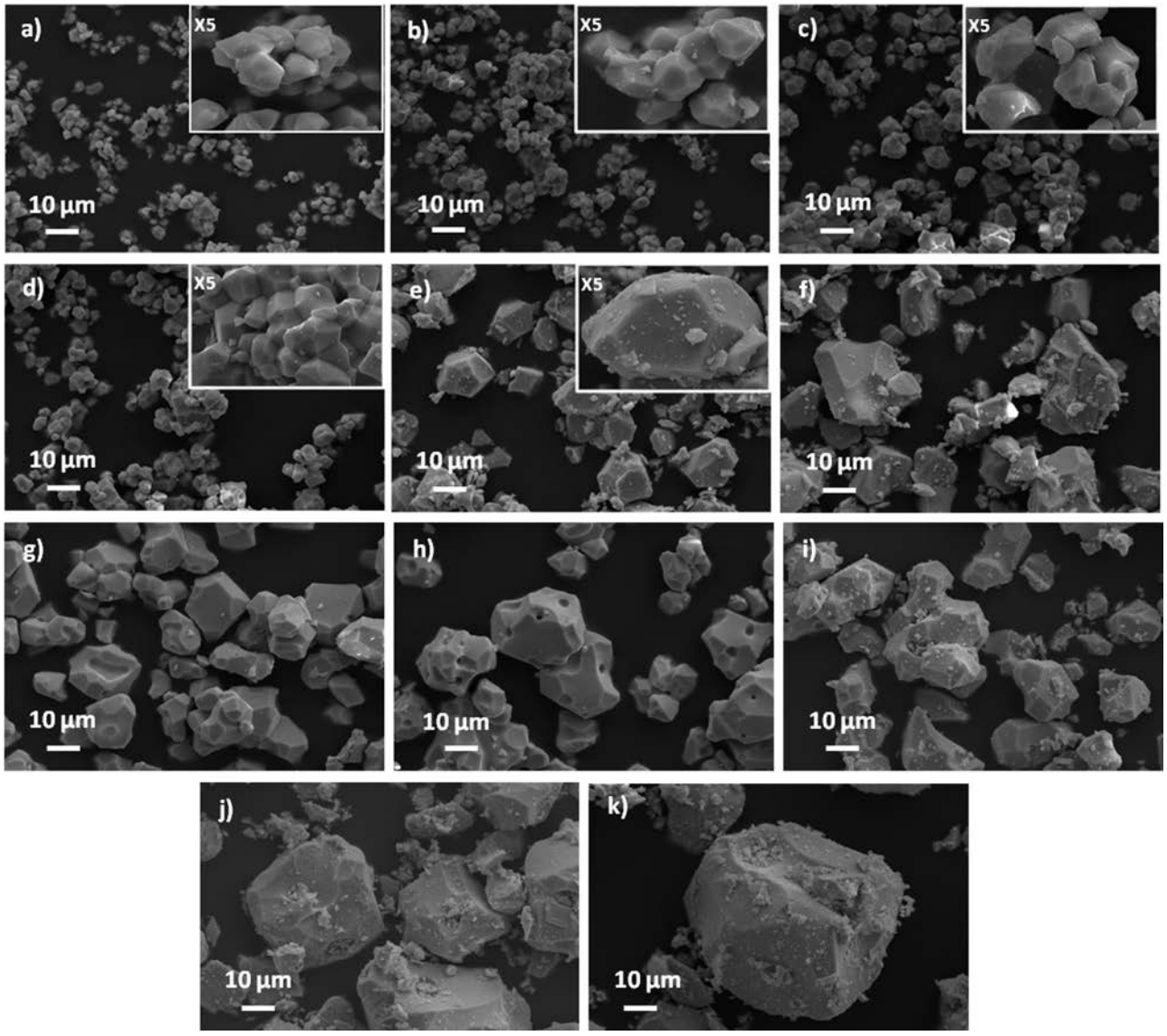

Fig. 8. a–k: Scanning electron microscopy analysis of the $Sr_{1-x}Pb_xMoO_4$ phase (a) x = 0, (b) x = 0.1, (c) x = 0.2, (d) x = 0.3, (e) x = 0.4, (f) x = 0.5, (g) x = 0.6, (h) x = 0.7, (i) x = 0.8, (j) x = 0.9 and (k) x = 1. In inset: magnification of images (x5).

the lattice [47]. Based on several measurements and studying the electronic structure of lead molybdate Dong and Wu suggested that the PL emission (band maximum at 400 nm) in $PbMoO_4$ nanobelts could be related to MoO_4^{2-} groups [92].

According to Babin et al., the green PL emission in $PbMoO_4$ crystals was attributed to an excitation in MoO_4^{2-} groups [93]. However, Van Loo proposed to attribute the blue luminescence in $PbMoO_4$ (2.7 eV) crystals to a transition in isolated MoO_4^{2-} groups, and the green luminescence (2.4 eV) to electron transfer between Pb6s orbital to 4d orbitals of Mo in MoO_4 groups [94–96]. Several authors confirmed the explanation by Groenink and Blasse who proposed that the $PbMoO_4$ emission (band maximum at 517 nm or 2.4 eV) could be assigned to the $^3T_1 \rightarrow {}^1A_1$ transition in the tetrahedral (MoO_4^{2-}) group. It is presumed that the $^3T_1$ level is split, due to spin-orbit coupling [91,92]. Chen and Gao argued that the green emission is a result of the intrinsic luminescent behavior

Table 4
SEM analyses. Evolution of grains size and EDX analyses for Sr, Pb and Mo atoms.

x	0	0.1	0.2	0.3	0.4	0.5	0.6	0.7	0.8	0.9	1
Medium size distribution	(2 ± 0.4)µm	(3 ± 0.6)µm	(5 ± 0.9)µm	(6 ±1)µm	(12 ± 2)µm	(15 ± 2)µm	(18 ± 3)µm	(19 ± 3)µm	(21 ± 3)µm	(24± 4)µm	(41 ± 7)µm
Secondary medium size distribution for small grain < 5 µm					(3 ± 0.5)µm	(3 ± 0.5)µm	(5 ± 0.9)µm	(6 ± 0.9)µm	(6 ± 1)µm	(6 ± 1)µm	(6 ± 1)µm
Sr (at%)	50.1	44.9	40.6	34.8	30.6	25.3	19.3	16.5	10.6	4.6	0.0
Pb (at%)	0.0	4.8	10.4	15.0	19.7	26.1	30.4	35.4	39.7	44.8	49.9
x_{exp}	0.0	0.1	0.21	0.30	0.39	0.52	0.61	0.71	0.79	0.89	1.00
Mo (at%)	49.9	49.7	51.0	50.0	48.5	49.0	47.5	48.7	44.2	49.6	51.3

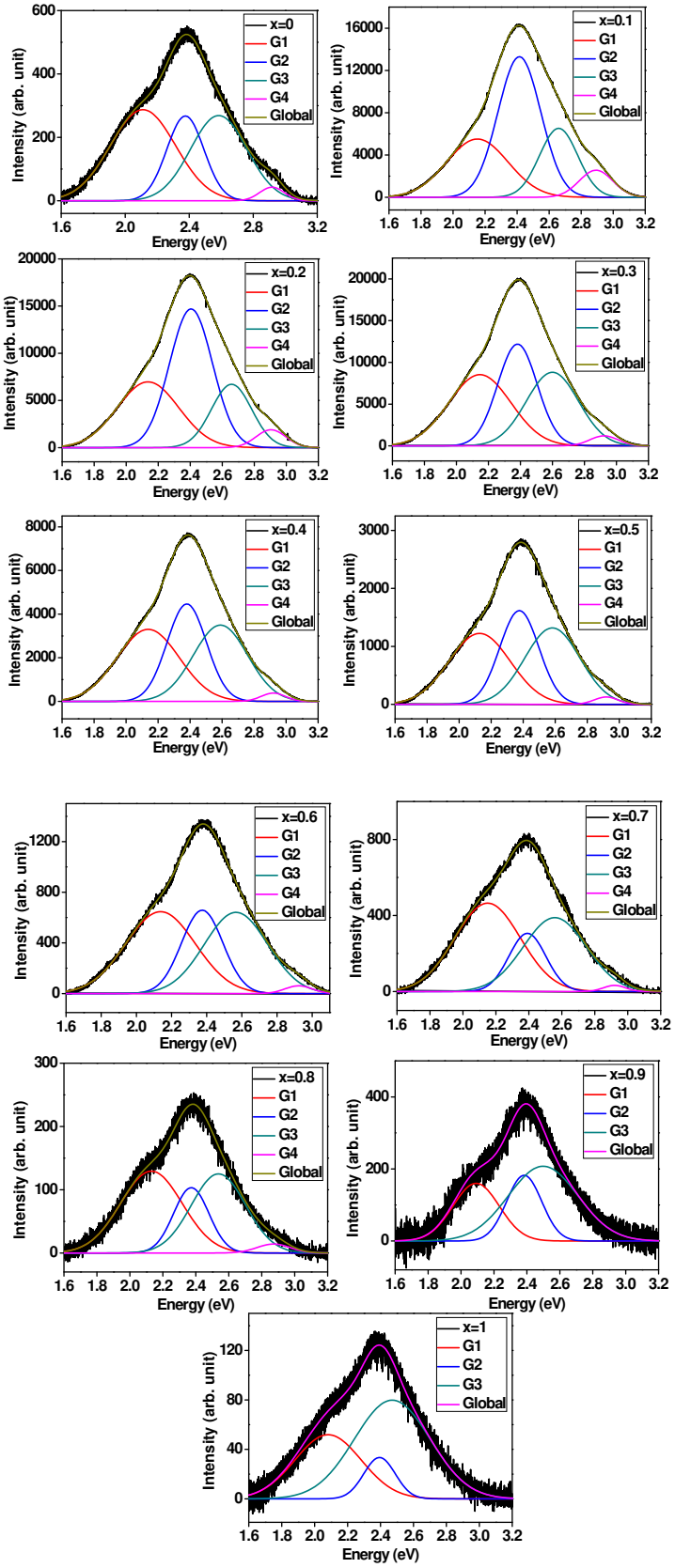

Fig. 9. a–k: Luminescence analyses on X-Ray excitation (45 kV; 35 A): Experimental emission bands of the $Sr_{1-x}Pb_xMoO_4$ polycrystalline phases with $0 \leq x \leq 1$. Four Gaussian components of all compositions are shown in the each figure.

of the MoO_4^{2-} group. These authors mentioned that the transition of the green luminescence is due to the $^3T_1,^3T_2 \rightarrow {}^1A_1$ transition in the tetrahedral molybdates group [93]. Based on these studies of the excitation and emission spectra, Bernhardt noted that the

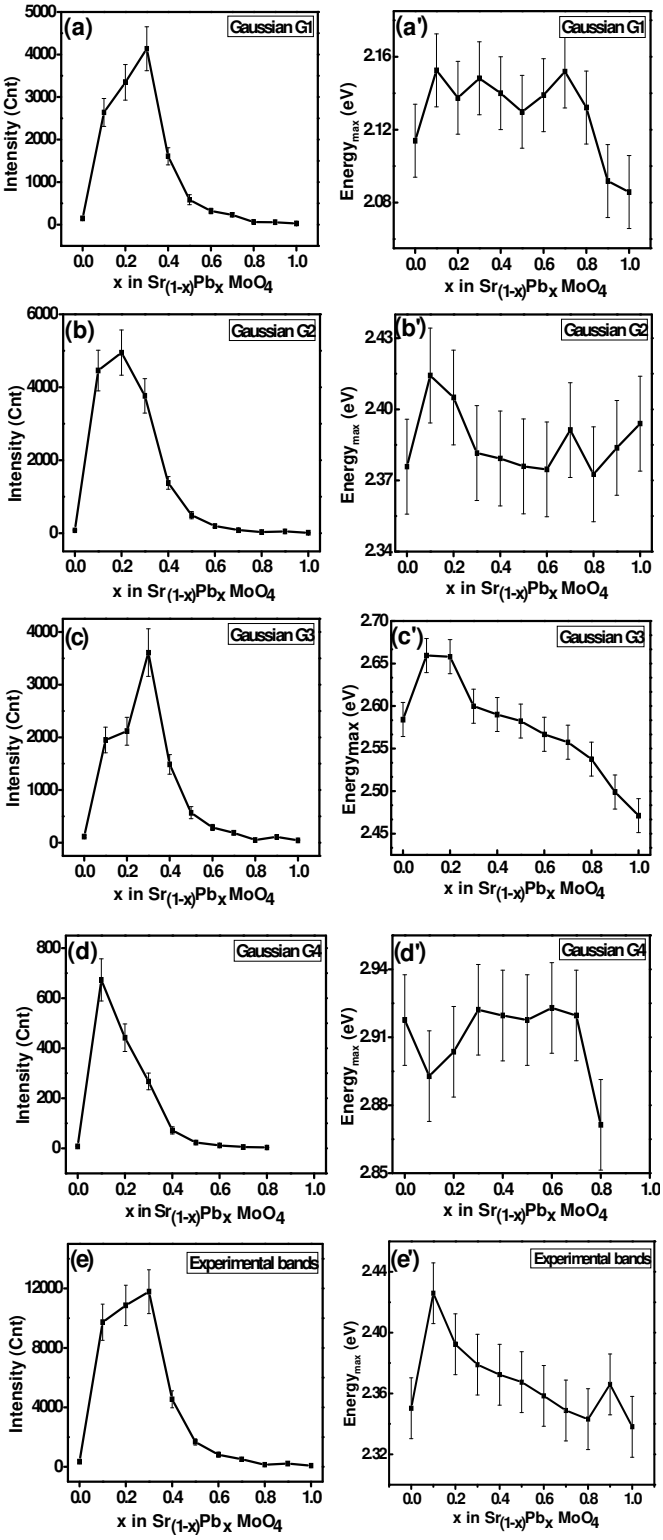

Fig. 10. The energies and integrated intensities of G_1, G_2, G_3 and G_4 components as a function of composition x.

yellow PL emission (band maximum at 600 nm or 2.1 eV) in $PbMoO_4$ crystals was temperature dependent [97]. Bomio et al. assumed that the PL properties of $PbMoO_4$ crystals were associated to surface defects and were mainly due to possible distortions on both distorted tetrahedron [MoO_4] and [PbO_8] clusters in the lattice [76].

In our experiments, the origin of the four components could be mainly due to the distortions of the MoO_4 and MO_8 groups. Only one component (G3) depends on composition x and presents a significant decrease with x in energy. This can be ascribed to the modifications of M-O-Mo links in relation with the modification of the covalence of Pb-O bonds, and the modification of Mo-O bonds

in tetrahedra. In addition, it should be noted that the small decrease of emission energies (Fig. 10e′) as x increases could be directly related to the expected decrease of band gap as a function of composition x.

The strong increase of PL intensities in the composition range x = 0.2 to x = 0.4 cannot be ascribed to the Pb content itself (contribution of Pb6s orbitals): it can be connected with the specific disorder of M-O-Mo links, involving distortions or rotations of tetrahedra MoO_4. A similar observation was done in our recent work on $Sr_{1-x}Pb_xWO_4$ solid solution with a maximum of PL intensity for compositions x close to 0.3. This maximum can be due to the compromise between the increase of number of emission centers and the increase of quenching (absorption) effect. In fact, if lead is assumed to be at the origin of the increasing number of emission centers, a maximum disorder of the Pb distribution in the lattice can be expected for the composition x = 0.5. However, with the increase of the Pb composition, the absorption effects, for incident photons as well as for emitted photons, necessarily increase, and thus, the maximum emission might be observed for a composition $x < 0.5$.

4. Conclusion

In summary, a series of molybdates $Sr_{(1-x)}Pb_xMoO_4$ ($0 \leq x \leq 1$) prepared at 1000 °C by the solid state method for 6 h. Rietveld refinements applied to XRD patterns of polycrystalline samples showed that a disordered solid solution with scheelite tetragonal structure was formed. The cell parameters linearly increased with Pb composition. The micro-Raman spectra confirmed the formation of a continuous solid solution, and a specific disorder was clearly evidenced through the modifications of the Raman bands at 794 (E_g) and 845 (B_g) cm^{-1} for $SrMoO_4$. The PL experiments under X-ray excitation were interpreted in terms of four gaussian components, with energies ranging between 2.1 (yellow) and 2.9 (violet) eV. These components are probably related to the distortions of tetrahedra directly involved by the disordered distribution of Sr-O-Mo and Pb-O-Mo links. These distortions might be at the origin of the splitting of PL transitions in irregular tetrahedra MoO_4. Finally, the major fact resides in the strong increase of PL intensities in the range $0.2 < x < 0.4$. This maximum could result from the compromise between the increasing numbrer of emission centers associated with Sr substitution by Pb, and a quenching effect of these emissions as Pb content increases. This observation is in agreement with the maximum of intensity close to the composition x = 0.3, observed in our recently studied series $Sr_{1-x}Pb_xWO_4$. In these two studies, the crystallite sizes and morphologies could not be invoked to interpret these abnormal variations of PL intensities.

Acknowledgments

This work was financially supported by the Regional: Council of Provence-Alpes – Côte d'Azur – France (Grant number: 2012-16322), the General Council of Var, Toulon Provence Mediterranean and conducted as part of the CNRS-CNRST 2014 project (Grant number: 02/14).

References

[1] A. Hallaoui, A. Taoufyq, M. Arab, B. Bakiz, A. Benlhachemi, L. Bazzi, S. Villain, J.-C. Valmalette, F. Guinneton, J.-R. Gavarri, J. Solid State Chem. 227 (2015) 186–195.
[2] A. Taoufyq, V. Mauroy, F. Guinneton, B. Bakiz, S. Villain, A. Hallaoui, A. Benlhachemi, G. Nolibe, A. Lyoussi, J.-R. Gavarri, Mater. Res. Bull. 70 (2015) 40–46.
[3] S.K. Ghosh, S.K. Rout, A. Tiwari, P. Yadav, J.C. Sczancoski, M.G.R. Filho, L.S. Cavalcante, J. Mater. Sci. Mater. Electron. 26 (2015) 8319–8335.
[4] Y. Zhang, F. Yang, J. Yang, Y. Tang, P. Yuan, Solid State Commun. 133 (2005) 759–763.
[5] P. Jena, S.K. Gupta, V. Natarajan, O. Padmaraj, N. Satyanarayana, M. Venkateswarlu, Mater. Res. Bull. 64 (2015) 223–232.
[6] M. Anicete-Santos, E. Orhan, M.A.M.A. de Maurera, L.G.P. Simões, A.G. Souza, P. S. Pizani, E.R. Leite, J.A. Varela, J. Andrés, A. Beltrán, E. Longo, Phys. Rev. B: Condens. Matter 75 (2007) 165105-1–165105-11.
[7] J.H. Ryu, J.-W. Yoon, K.B. Shim, Solid State Commun. 133 (2005) 657–661.
[8] A. Kaddouri, E. Tempesti, C. Mazzocchia, Mater. Res. Bull. 39 (2004) 695–706.
[9] J.H. Ryu, J.-W. Yoon, C.S. Lim, W.-C. Oh, K.B. Shim, J. Alloys Compd. 390 (2005) 245–249.
[10] A.P.A. Marques, D.M.A. de Melo, C.A. Paskocimas, P.S. Pizani, M.R. Joya, E.R. Leite, E. Longo, J. Solid State Chem. 179 (2006) 671–678.
[11] J. Kubo, W. Ueda, Mater. Res. Bull. 44 (2009) 906–912.
[12] H. Fu, J. Lin, L. Zhang, Y. Zhu, Appl. Catal. A Gen. 306 (2006) 58–67.
[13] A.M.E.S. Raj, C. Mallika, O.M. Sreedharan, K.S. Nagaraja, Mater. Lett. 53 (2002) 316–320.
[14] R. Sundaram, K.S. Nagaraja, Mater. Res. Bull. 39 (2004) 581–590.
[15] R.C. Pullar, S. Farrah, N.M. Alford, J. Eur. Ceram. Soc. 27 (2007) 1059–1063.
[16] G. Zhang, R. Jia, Q. Wu, Mater. Sci. Eng. B 128 (2006) 254–259.
[17] T. Thongtem, S. Kungwankunakorn, B. Kuntalue, A. Phuruangrat, S. Thongtem, J. Alloys Compd. 506 (2010) 475–481.
[18] Z. Shahri, M. Bazarganipour, M. Salavati-Niasari, Superlattices Microstruct. 63 (2013) 258–266.
[19] S.W. Park, B.K. Moon, J.H. Jeong, J.S. Bae, J.H. Kim, Mater. Res. Bull. 70 (2015) 403–411.
[20] T. Gholami, M. Salavati-Niasari, M. Bazarganipour, E. Noori, Superlattices Microstruct. 61 (2013) 33–41.
[21] P. Du, J.S. Yu, Mater. Res. Bull. 70 (2015) 553–558.
[22] M. Salavati-Niasari, B. Shoshtari-Yeganeh, M. Bazarganipour, Superlattices Microstruct. 58 (2013) 20–30.
[23] E. Noori, M. Salavati-Niasari, M. Bazarganipour, T. Gholami, J. Cluster Sci. 24 (2013) 1171–1180.
[24] J. Bi, C.-H. Cui, X. Lai, F. Shi, D.-J. Gao, Mater. Res. Bull. 43 (2008) 743–747.
[25] M. Sletnes, J.C. Valmalette, T. Grande, M.-A. Einarsrud, J. Solid State Chem. 233 (2016) 30–36.
[26] M. Sletnes, M. Lindgren, J.C. Valmalette, N.P. Wagner, T. Grande, M.-A. Einarsrud, J. Solid State Chem. 237 (2016) 72–80.
[27] A. Phuruangrat, T. Thongtem, S. Thongtem, J. Ceram. Soc. Jpn. 116 (2008) 605–609.
[28] L.S. Cavalcante, J.C. Sczancoski, R.L. Tranquilin, M.R. Joya, P.S. Pizani, J.A. Varela, E. Longo, J. Phys. Chem. Solids 69 (2008) 2674–2680.
[29] L.S. Cavalcante, J.C. Sczancoski, J.W.M. Espinosa, J.A. Varela, P.S. Pizani, E. Longo, J. Alloys Compd. 474 (2009) 195–200.
[30] L.S. Cavalcante, J.C. Sczancoski, L.F. Lima Jr., J.W.M. Espinosa, P.S. Pizani, J.A. Varela, E. Longo, Cryst. Growth Des. 9 (2009) 1002–1012.
[31] J.C. Sczancoski, L.S. Cavalcante, M.R. Joya, J.A. Varela, P.S. Pizani, E. Longo, Chem. Eng. J. 140 (2008) 632–637.
[32] K. Teshima, K. Yubuta, S. Sugiura, Y. Fujita, T. Suzuki, M. Endo, T. Shishido, S. Oishi, Cryst. Growth Des. 6 (2006) 1598–1601.
[33] V.B. Mikhailik, H. Kraus, G. Miller, M.S. Mykhaylyk, D. Wahl, J. Appl. Phys. 97 (2005) 083523-1–083523-8.
[34] H.C. Zeng, J. Cryst. Growth 160 (1996) 119–128.
[35] L.B. Barbosa, D.R. Ardila, C. Cusatis, J.P. Andreeta, J. Cryst. Growth 235 (2002) 327–332.
[36] Z. Shahri, A. Sobhani, M. Salavati-Niasari, Mater. Res. Bull. 48 (2013) 3901–3909.
[37] Z. Shahri, M. Salavati-Niasari, N. Mir, G. Kianpour, J. Cryst. Growth 386 (2014) 80–87.
[38] D. Chen, K. Tang, F. Li, H. Zheng, Cryst. Growth Des. 6 (2006) 247–252.
[39] T. Thongtem, S. Kungwankunakorn, B. Kuntalue, A. Phuruangrat, S. Thongtem, J. Alloys Compd. 506 (2010) 475–481.
[40] G. Kianpour, M. Salavati-Niasari, H. Emadi, Superlattices Microstruct. 58 (2013) 120–129.
[41] G. Kianpour, M. Salavati-Niasari, H. Emadi, Ultrason. Sonochem. 20 (2013) 418–424.
[42] K. Saberyan, F. Soofivand, G. Kianpour, M. Salavati-Niasari, S. Bagheri, J. Mater. Sci: Mater. Electron. (2015) 1–8.
[43] J.H. Ryu, J.-W. Yoon, C.S. Lim, W.-C. Oh, K.B. Shim, J. Alloy Compd. 390 (2005) 245–249.
[44] J.H. Ryu, S.-M. Koo, J.-W. Yoon, C.S. Lim, K.B. Shim, Mater. Lett. 60 (2006) 1702–1705.
[45] Y. Liu, Y. Chu, Mater. Chem. Phys. 92 (2005) 59–63.
[46] F. Lei, B. Yan, J. Solid State Chem. 181 (2008) 855–862.
[47] J.C. Sczancoski, M.D.R. Bomio, L.S. Cavalcante, M.R. Joya, P.S. Pizani, J.A. Varela, J. Phys. Chem. C 113 (2009) 5812–5822.
[48] M.R.D. Bomio, R.L. Tranquilin, F.V. Motta, C.A. Paskocimas, R.M. Nascimento, L. Gracia, J. Phys. Chem. C 117 (2013) 21382–21395.
[49] Y. Cheng, Y. Wang, D. Chen, F. Bao, J. Phys. Chem. B 109 (2004) 794–798.
[50] M. Shen, Q. Zhang, H. Chen, T. Peng, CrystEngComm 13 (2011) 2785–2791.
[51] C. Zhang, E. Shen, E. Wang, Z. Kang, L. Gao, C. Hu, L. Xu, Mater. Chem. Phys. 96 (2006) 240–243.
[52] N. Niu, P. Yang, W. Wang, F. He, S. Gai, D. Wang, J. Lin, Mater. Res. Bull. 46 (2011) 333–339.
[53] Q. Gong, X.F. Qian, X.D. Ma, Z.K. Zhu, Cryst. Growth Des. 6 (2006) 1821–1825.

[54] H. Alves, A. Hofstaetter, F. Leiter, B.K. Meyer, N.G. Romanov, R. Novotny, Radiat. Meas. 33 (2001) 641–644.
[55] G.J. Xing, R. Liu, C. Zhao, Y.-L. Li, Y. Wang, G.-M. Wu, Ceram. Int. 37 (2011) 2951–2956.
[56] S. Lei, X. Peng, X. Li, Z. Liang, Y. Yang, B. Cheng, Y. Xiao, L. Zhou, Mater. Res. Bull. 46 (2011) 601–608.
[57] Z.H. Li, J.M. Du, J.L. Zhang, T.C. Mu, Y.N. Gao, B.X. Han, J. Chen, J.W. Chen, Mater. Lett. 59 (2005) 64–68.
[58] D. Chen, G. Shen, K. Tang, Z. Liang, H. Zheng, J. Phys. Chem. B 108 (2004) 11280–11284.
[59] A. Phuruangrat, T. Thongtem, S. Thongtem, J. Cryst. Growth 311 (2009) 4076–4081.
[60] P. Kwolek, T. Tokarski, T. Lokcik, K. Szacilowski, Arch. Metall. Mater. 58 (2013) 217–222.
[61] H.C. Zeng, J. Mater. Res. 11 (1996) 703–715.
[62] Z.L. Wang, H.B. Liang, M.L. Gong, Q. Su, Opt. Mater. 29 (2007) 896–900.
[63] K. Teshima, K. Yubuta, S. Sugiura, Y. Fujita, T. Suzuki, M. Endo, T. Shishido, S. Oishi, Cryst. Growth Des. 6 (2006) 1598–1601.
[64] V.B. Mikhailik, H. Kraus, G. Miller, M.S. Mykhaylyk, D. Wahl, J. Appl. Phys. 97 (2005) 083523–083523-8.
[65] A. Phuruangrat, T. Thongtem, S. Thongtem, J. Alloys Compd. 481 (2009) 568–572.
[66] F. Lei, B. Yan, J. Solid State Chem. 181 (2008) 855–862.
[67] J.H. Ryu, B.G. Choi, J.W. Yoon, K.B. Shim, K. Machi, K. Hamada, J. Lumin. 124 (2007) 67–70.
[68] A. Taoufyq, F. Guinneton, J.-C. Valmalette, M. Arab, A. Benlhachemi, B. Bakiz, S. Villain, A. Lyoussi, G. Nolibe, J.-R. Gavarri, J. Solid State Chem. 219 (2014) 127–137.
[69] V.D. Zhuravlev, E.V. Tkachenko, N.A. Laishevtseva, L.M. Fedorova, V.T. Gabriehlyan, Žurnal neorganičeskoj himii (in Russian) 30 (1985) 763–765.
[70] Proceedings of the Seventh European Powder Diffraction Conference, in: T. Roisnel, J. Rodríguez-Carvajal, R. Delhez, E.J. Mittenmeijer (Eds.), Barcelona, 2000, pp. 118–123.
[71] H.M. Rietveld, Acta Crystallogr. 22 (1967) 151–152.
[72] H.M. Rietveld, J. Appl. Crystallogr. 2 (1969) 65–71.
[73] S.K. Pradhan, S. Bid, M. Gateshki, V. Petkov, Mater. Chem. Phys. 93 (2005) 224–230.
[74] S. Bid, S.K. Pradhan, J. Appl. Crystallogr. 35 (2002) 517–525.
[75] V.K. Pecharsky, P.Y. Zavalij, Springer Science & Business Media (2005) 512–513.
[76] I.C. Nogueira, L.S. Cavalcante, P.F.S. Pereira, M.M. de Jesus, J.M. Rivas Mercury, N.C. Batista, M. Siu Li, E. Longo, J. Appl. Cryst. 46 (2013) 1434–1446.
[77] E. Gurmen, E. Daniels, J.S. Kin, J. Chem. Phys. 55 (1971) 1093–1097.
[78] M.R.D. Bomio, L.S. Cavalcante, M.A.P. Almeida, R.L. Tranquilin, N.C. Batista, P.S. Pizani, M. Siu Li, J. Andres, E. Longo, Polyhedron 50 (2013) 532–545.
[79] M. Crane, R.L. Frost, P.A. Williams, J.T. Kloprogge, J. Raman Spectrosc. 33 (2002) 62.
[80] D. Christofilos, G.A. Kourouklis, S. Ves, J. Phys. Chem. Solids 56 (1995) 1122.
[81] D.L. Rousseau, R.P. Bauman, S.P.S. Porto, J. Raman Spectrosc. 10 (1981) 253–290.
[82] H.S. Lee, S.D. Lee, J.H. Lee, M.S. Jang, Ferroelecrrics 107 (1990) 151–154.
[83] E. Reut, Izv. Akad. Nauk SSSR, Ser. Fiz (in Russian) 43 (1979) 1186–1193.
[84] J.W. Yoon, J.H. Ryu, K.B. Shim, Mater. Sci. Eng. B 127 (2006) 154–158.
[85] D.A. Spasskya, S.N. Ivanov, S.N. Kolobanov, V.V. Mikhailin, V.N. Zemskov, B.I. Zadneprovski, L.I. Potkin, Radiat. Meas. 38 (2004) 607–610.
[86] J. Bi, L. Wu, Y. Zhang, Z. Li, J. Li, X. Fu, Appl. Catal. B 91 (2009) 135–143.
[87] Y. Shimodaira, H. Kato, H. Kobayashi, A. Kudo, Bull. Chem. Soc. Jpn. 80 (2007) 885–893.
[88] M. Bacci, S. Porcinai, E. Mihokova, M. Nikl, K. Polak, Phys. Rev. B 64 (2001) 104302-1–104302-6.
[89] J.A. Groenink, G. Blasse, J. Solid State Chem. 32 (1980) 9–20.
[90] G. Blasse, Struct. Bond. 42 (1980) 01–41.
[91] L. Chen, Y. Gao, Chem. Eng. J. 131 (2007) 181–185.
[92] F.Q. Dong, Q.-S. Wu, Appl. Phys. A 91 (2008) 161–165.
[93] V. Babin, P. Bohacek, E. Bender, A. Krasnikov, E. Mihokova, M. Nikl, N. Senguttuvan, A. Stolovits, Y. Usuki, S. Zazubovich, Radiat. Meas. 38 (2004) 533–537.
[94] W. Van Loo, Phys. Status Solidi A 27 (1975) 565–574.
[95] W. Van Loo, J. Lumin. 10 (1975) 221–235.
[96] W. Van Loo, Phys. Status Solidi A 28 (1975) 227–235.
[97] H. Bernhardt, Phys. Status Solidi A 91 (1985) 643–648.